JBC RESEARCH ARTICLE

Tryptophan mutations in G3BP1 tune the stability of a cellular signaling hub by weakening transient interactions with Caprin1 and USP10

Received for publication, March 11, 2022, and in revised form, September 20, 2022 Published, Papers in Press, September 29, 2022,
https://doi.org/10.1016/j.jbc.2022.102552

Colin T. Sheehan[1], **Thomas H. Hampton**[2], **and Dean R. Madden**[1,*]

From the [1]*Department of Biochemistry and Cell Biology, and* [2]*Department of Microbiology and Immunology, Geisel School of Medicine at Dartmouth, Hanover, New Hampshire, USA*

Edited by Wolfgang Peti

Intrinsically disordered proteins (IDPs) often coordinate transient interactions with multiple proteins to mediate complex signals within large protein networks. Among these, the IDP hub protein G3BP1 can form complexes with cytoplasmic phosphoprotein Caprin1 and ubiquitin peptidase USP10; the resulting control of USP10 activity contributes to a pathogenic virulence system that targets endocytic recycling of the ion channel CFTR. However, while the identities of protein interactors are known for many IDP hub proteins, the relationship between pairwise affinities and the extent of protein recruitment and activity is not well understood. Here, we describe *in vitro* analysis of these G3BP1 affinities and show tryptophan substitutions of specific G3BP1 residues reduce its affinity for both USP10 and Caprin1. We show that these same mutations reduce the stability of complexes between the full-length proteins, suggesting that copurification can serve as a surrogate measure of interaction strength. The crystal structure of G3BP1 TripleW (F15W/F33W/F124W) mutant reveals a clear reorientation of the side chain of W33, creating a steric clash with USP10 and Caprin1. Furthermore, an amino-acid scan of USP10 and Caprin1 peptides reveals similarities and differences in the ability to substitute residues in the core motifs as well as specific substitutions with the potential to create higher affinity peptides. Taken together, these data show that small changes in component binding affinities can have significant effects on the composition of cellular interaction hubs. These specific protein mutations can be harnessed to manipulate complex protein networks, informing future investigations into roles of these networks in cellular processes.

Intrinsically disordered proteins (IDPs) are important molecular machines that play critical roles in cellular processes and signaling pathways (1, 2). Such proteins lack a well-defined three-dimensional globular structure and can range from fully to partially unstructured. This stereochemical flexibility allows these proteins to interact promiscuously with different proteins in a context-dependent manner (3). Additionally, these proteins often utilize conserved sequence motifs to facilitate protein–protein interactions with high specificity and modest affinity, leading to rapid signal transduction (4–6). IDPs often function as interaction hubs as well as facilitators of biomolecular condensation. Ras GTPase Activating Protein SH3 Domain Binding Protein 1 (G3BP1), a protein containing many intrinsically disordered regions, is reported to serve as an interaction hub in stress granules (SGs) and to form transient interactions with ubiquitin-specific peptidase 10 (USP10) and cytoplasmic activating/proliferation associated protein 1 (Caprin1), which in turn influence the SG network organization and signaling (7–9).

G3BP1 is a 52 kDa protein ubiquitously expressed in the cytoplasm. Current research supports the theory that the main role of G3BP1 is to selectively modulate mRNA stability in response to intracellular and extracellular stimuli. However, significant evidence suggests that G3BP1 plays a central role in several additional cellular processes, including rasGAP signaling, ubiquitination, mRNA metabolism, and SG formation, and these diverse functions appear to be modulated by G3BP1's interaction with RNA and other proteins (10–18). The large protein network surrounding G3BP1 has been implicated in several diseases including neurological and neurodegenerative disorders, cancer progression, bacterial pathogenesis, and viral infection (14, 16, 17, 19, 20). The ability to selectively modulate protein–protein interactions within this large, intricate protein network would represent a novel drug target with far reaching implications (21–24).

G3BP1 and the other two members of the G3BP family all share the following five domains: an N-terminal nuclear transport factor 2-like domain (NTF2), a central region consisting of several proline-rich (PxxP) motifs, an acid-rich domain, a canonical RNA recognition motif, and a loosely conserved C-terminal arginine- and glycine-rich (RGG) box (25). Except for the NTF2-like domain and RNA-binding domain, G3BP proteins are predicted to be largely disordered. A recently reported model suggests that interactions with RNA and proteins partners modulate the structure and provide relative stability to G3BP1 (8, 9).

The NTF2 domain is the most highly conserved domain in the G3BP family and plays a role in several G3BP functions including dimerization, protein binding, and SG formation

* For correspondence: Dean R. Madden, dean.r.madden@dartmouth.edu.

(13, 26, 27). Proteins known to interact with G3BP1 NTF2 include rasGAP, Caprin1, and USP10 (10, 15, 28). Multiple groups have shown that Caprin1 and USP10 compete for the same binding groove on the G3BP1 NTF2 domain (7, 8, 29). Recent G3BP1 NTF2 cocrystal structures have identified three phenylalanine residues (F15, F33, and F124) that are responsible for coordinating peptides from Caprin1 and USP10 (26, 30). Additionally, several groups have shown that mutating F33 to a tryptophan ablates Caprin1 and USP10 binding (8, 26, 31, 32).

USP10 is an 87 kDa cysteine protease and a member of the deubiquitinating enzyme (DUB) family. As a DUB family member, USP10 plays an important role in protein homeostasis and has been shown to remove conjugated ubiquitin from targets like p53/TP53, BECN1, SNX3, and the cystic fibrosis transmembrane conductance regulator (CFTR) (33–36). Additionally, USP10 has been implicated in a variety of diseases, including cancer, where it can act as an oncogene or a tumor suppressor, as well as Alzheimer's disease and other neurodegenerative diseases (19, 37–40).

USP10 contains a highly conserved catalytic domain (USP domain) beginning at residue R415 and spanning most of the C-terminal end of the protein. Similar to G3BP, the N-terminal half of the protein is predicted to be mostly disordered. First identified as a G3BP-interacting protein in a yeast two-hybrid screen, subsequent reports have identified a core motif (FGDF; residues 10–13) in USP10 that is recognized by G3BP1 NTF2 (15, 29). A cocrystal structure of NTF2 complexed with FGDF-containing peptides revealed that both motif phenylalanine residues (F10 and F13) protrude into the NTF2-binding grove and form π-stacking interactions with NTF2 residues F15, F33, and F124 (26, 32). Alanine substitution of USP10 F10, G11, or F13 completely ablates G3BP1 binding, while D12A allows for weak binding (32). These data show that the FGDF is necessary and sufficient for G3BP1 binding.

Caprin1 is a 78 kDa cytoplasmic RNA-binding protein. Caprin1 has been implicated in cell cycle regulation and cell proliferation where it acts alone or in combination with other RNA-binding proteins such as G3BP1 and fragile X mental retardation protein (28, 41–44). Caprin1 binds RNA *via* its C-terminal RNA-binding RGG motif and an RG enrichment region (28). Caprin1 contains a highly conserved F(M/I/L)Q(D/E)Sz(I/L)D motif spanning residues 372 to 379 that is recognized by G3BP1 NTF2 (28). A recent cocrystal structure revealed that the Caprin1 YNFI(Q) segment binds in the same hydrophobic grove on NTF2 as the USP10 FGDF motif (30). The structure further highlighted the important role of NTF2 residues F15, F33, and F124 in coordinating Caprin1 and USP10 peptides.

G3BP1 and its interactions with USP10 and Caprin1 are important for SG formation and regulation. Additionally, USP10 and Caprin1 have distinct roles in several cellular processes separate from G3BP1 and SGs (28, 33, 34, 45, 46). However, there is limited information on the importance of specific conserved motifs for the stability of IDP interactions. We therefore sought to better understand the interaction of these proteins at the residue level and to generate better tools for future investigations. We report here the first crystal structure of G3BP1 NTF2 harboring three phenylalanine substitutions in residues F15, F33, and F124 (TripleW). Additionally, we show a full amino-acid scan of the USP10 and Caprin1 binding-motif peptides and correlate these results with cellular protein association *via* copurification assays.

Results

G3BP1 phenylalanine residues contribute differentially to USP10 binding

The highly conserved G3BP1 NTF2 domain binds peptide motifs from USP10 (15, 28, 29). To further understand the contribution of specific residues in the G3BP1-binding groove to the interaction, we established a binding assay using fluorescence polarization (FP). The G3BP1 NTF2 domain spanning residues 1 to 139 was recombinantly expressed and purified from *E. coli*. Using a USP10-derived octameric reporter peptide (*F**-YI**FGDF**SP; *F**, fluorescein-aminohexanoic acid tag) containing the core FGDF motif, a binding isotherm was determined for WT-NTF2 (Fig. 1*A*). The experimental isotherm was fit by non-linear least squares to a single site–binding curve, yielding an equilibrium dissociation constant (K_D) (see Table 1). The value for the USP10 peptide is 2-fold stronger than the previously reported NTF2 K_D value of 7 μM for an FGDF-containing nsP3 peptide (32) and 30-fold stronger than the 115 μM value reported for a DSGFSFGSK peptide (27).

Having established a robust and repeatable assay using several different batches of NTF2, we next sought to test the effects of mutation on binding affinity. Residues F15, F33, and F124 in NTF2 are reported to play a role in coordinating the FGDF peptide from USP10 (17, 26, 32), so we focused our investigation on these residues, mutating resides F15, F33, and F124 to tryptophan (29, 32), singly and in combinations. Additional constructs were created to test other amino-acid mutations for these three residues, including alanine and tyrosine, but most of these constructs had low expression or produced insoluble protein when introduced in combination and thus were not included in our analyses. Substitutions of tryptophan for F15 or F33 yielded 3.5- and 7.5-fold decreases in affinity, respectively (Table 1). By itself, the F124W mutant caused no significant change in binding affinity. A linear mixed-effects model revealed that the contributions of F15W (p = 0.0001) and F33W (p = 0.000001) to binding affinity are each statistically significant, whereas F124W is not (p = 0.25). This agrees with multiple reports that G3BP1 harboring a F33W mutation is deficient in USP10 complex formation, whereas F124W has no effect on complex formation (26, 31, 32).

Next, we created double and triple mutants to see if the effects of the single substitutions were additive. NTF2 F15/33W and F33/124W exhibited significant increases in K_D values compared to either of the component single mutants. However, NTF2 F15/124W was only modestly worse than F15W alone. The most potent mutant was NTF2 TripleW with a K_D of 172.3 μM, although it was only modestly worse than

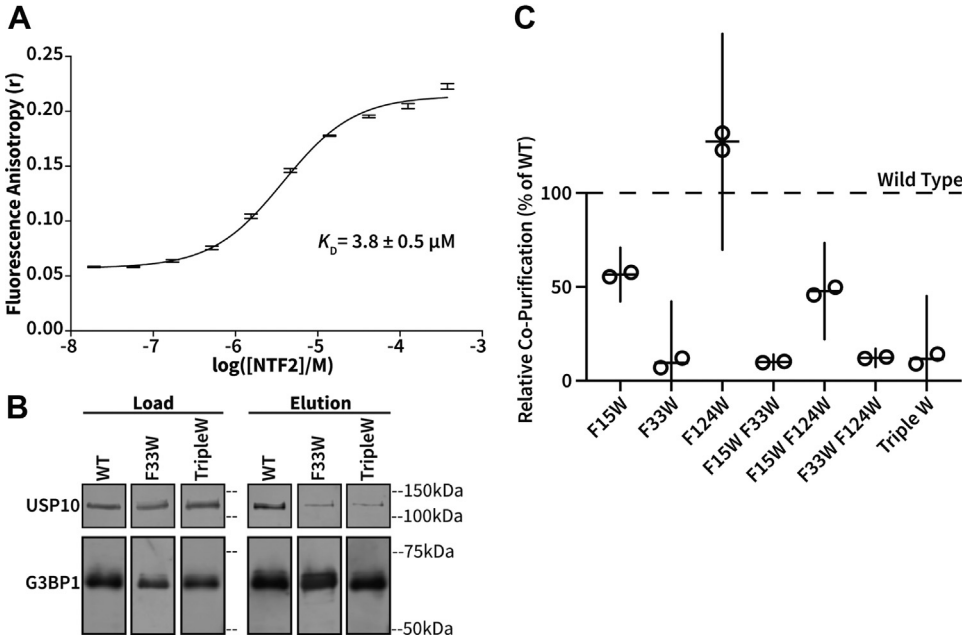

Figure 1. Individual equilibrium dissociation constants and copurification of G3BP1:USP10 interactions. *A*, an NTF2:USP10 binding isotherm was determined from fluorescence polarization assays. Fluorescence anisotropy data were collected using increasing concentrations of G3BP1 NTF2 in the presence of 30 nM reporter peptide derived from the USP10 FGDF binding motif (Fluorescein-aminohexanoic acid[*F**]-YIFGDFSP). Data are shown as mean ± standard deviation of n = 3 experiments. Average values were fit using a non-linear least-squares algorithm to determine K_D. *B*, Expi293 cells were transfected with plasmids expressing His-G3BP1 WT or mutant constructs, and lysates were subjected to affinity purification to recover His-tagged G3BP1. Equal fractions of load (*left*) and eluates (*right*) were run on SDS-PAGE followed by immunoblotting with anti-G3BP1 (*bottom*) and anti-USP10 (*top*) antibodies. *C*, immunoblots were analyzed *via* Image Studio, and mutants were compared to WT. Data presented as individual values of n = 2 experiments and 95% confidence intervals (*vertical bars*).

F15/33W. These data suggest that the contribution of F124 to USP10 peptide binding is much less than might be expected based on earlier cocrystal structures (17, 26). In addition, our linear mixed-effects model of binding affinities showed no evidence for a statistically significant interaction (p = 0.24) between F15W and F33W, confirming that they most likely act in an independent and additive fashion.

Our FP experiments revealed that we could manipulate the equilibrium dissociation constant of NTF2 and USP10 peptide across almost two orders of magnitude using specific tryptophan substitutions. However, we also wanted to test the effect these mutations would have on the ability of full-length versions of G3BP1 and USP10 to interact and form complexes in a cellular context. We recombinantly expressed His-tagged full-length G3BP1 in Expi293 cells, performed immobilized metal-affinity purification, and noticed that the same molecular weight bands were copurifying across many optimization trials (Fig. S1). We performed Western blot analysis on the first fraction and determined that USP10 and Caprin1 were copurifying with G3BP1 (Fig. 1*B*).

Table 1
USP10:G3BP1-NTF2 affinities

NTF2 construct	K_D (μM)
WT	3.8 ± 0.5
F15W	13.2 ± 0.9
F33W	28.4 ± 1.1
F124W	3.9 ± 0.5
F15/33W	144.2 ± 3.9
F15/124W	12.2 ± 0.8
F33/124W	68.4 ± 8.4
TripleW	172.3 ± 5.7

K_D values were derived by non-linear least-squares fitting of the mean and SD values from three independent FP titrations (see Fig. S2).

We decided to use this overexpression and affinity capture system to assay for binding stability of G3BP1 mutants. Copurification of USP10 was reduced by ∼90% when G3BP1-F33W was expressed instead of WT G3BP1 (Fig. 1*C*). Expression of any double or triple mutant including F33W (*e.g.*, G3BP1-F15/33W, G3BP1-F33/124W, and G3BP1-TripleW) caused a similar reduction in USP10 copurification. Expression and purification of G3BP1-F15W revealed a ∼44% reduction in USP10 copurification, whereas expression of the G3BP1-F15/124W double mutant caused a ∼53% reduction. As shown by the 95% confidence intervals in Figure 1*C*, all of these differences from WT levels are statistically significant. The G3BP1-F124W single mutant actually displayed a modest but statistically insignificant increase in USP10 copurification compared to WT, consistent with the observation that F124W does not significantly disrupt the equilibrium dissociation constant. A linear mixed-effects model of copurification confirms that the effects of F15W (p = 0.02) and F33W (p = 0.02), but not F124W (p = 0.8), are statistically significant and that the effects of F15W and F33W are most likely independent, that is, additive. When the degree of copurification for each mutant is plotted as a function of the associated K_D, it is evident that changes in binding affinity of G3BP1 NTF2 domains for the USP10 FGDF peptide correlate with changes in full-length G3BP1–USP10 complex stability (Fig. 2; blue). Residues F15, F33, and F124 each help to stabilize the interaction with USP10 but to a significantly different degree.

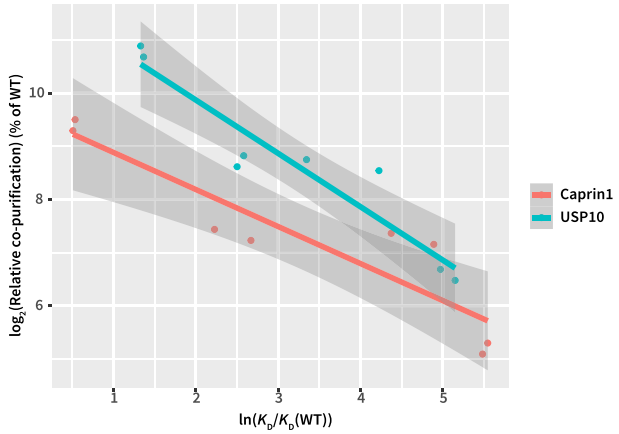

Figure 2. Comparison of relative copurification of endogenous USP10 or Caprin1 *versus* corresponding equilibrium dissociation constants for G3BP1 mutants. Full-length His-G3BP1constructs were overexpressed and affinity purified, and relative copurification percentages were calculated as described in Figures 1 and 3. Equilibrium dissociation constants (K_D) were calculated by fluorescence polarization assays using G3BP1 NTF2 (1–139) and USP10 or Caprin1 reporter peptides. Each point represents the relative copurification percentage and K_D for a G3BP1$_{mutant}$:USP10 (*blue*) or G3BP1$_{mutant}$:Caprin1 (*orange*) interaction. The lines represent linear fits to the observed data for each partner (*blue* = USP10; *orange* = Caprin1), and the *gray* corridors shown on either side of the lines represent 95% confidence intervals associated with the fit. The vertical offset between the two lines is significant (p = 0.007). For errors associated with the individual data points, see Figures 1 and 3 and Tables 1 and 2.

Caprin1 is more sensitive than USP10 to G3BP1 NTF2 modifications

Caprin1 competes with USP10 in binding the NTF2 domain; however, Caprin1 lacks an FGDF motif (29). Solomon *et al.* (28) reported that Caprin1 contains a conserved binding motif, FIQDSMLD, spanning residues 372 to 379. Given the differences in peptide-recognition sequences, we wanted to determine whether the three phenylalanine residues (F15, F33, and F124) identified as USP10 modulators also participate in binding and coordinating the Caprin1 peptide. We created a Caprin1-derived dodecamer reporter peptide (*F**-YN**FIQDSMLD**FE) to be used in FP assays. Using recombinant NTF2 and the Caprin1 reporter peptide, we generated a binding isotherm that could be fit to a single-site binding curve, yielding an estimate of the equilibrium dissociation constant (Fig. 3*A* and Table 2).

Our value is approximately 2.2-fold stronger than the K_D calculated for USP10. This result disagrees with a recent publication from Schulte *et al.* (30), which reported a stronger interaction between USP10:NTF2 than between Caprin1:NTF2 in isothermal titration calorimetry experiments. One possible explanation for this discrepancy is the pH: Schulte *et al.* used pH 7.5, whereas we used pH 8.5 in our experiments. G3BP1 residues H31 and H62 have been implicated in Caprin1 binding and have predicted pK_a values of 6.1 and 6.2, respectively. Depending on the local pK_a of the histidine side chains, they could be differentially protonated at pH 7.5 or pH 8.5. However, in our hands, preliminary measurements at pH 7.4 and 8.5 yielded similar K_D estimates (3.4 μM in each case). Alternatively, this discrepancy could be explained by the construct design, as the isothermal titration calorimetry experiments used longer (∼30 aa) USP10 and Caprin1 peptides. If correct, this suggests that residues outside of canonical binding motifs may also contribute to these protein interactions. Indeed, our peptide-array binding data surveyed the role of peptide length (Fig. S6). The longest peptides actually showed modestly weaker interactions than our shorter motif peptides, with a slightly greater diminution observed for Caprin1. Strict quantitation would require an analysis of peptide synthesis yields in each spot. Nonetheless, these observations suggest that construct length may account for the differences, whose absolute magnitude is small.

Mutation of F15 or F33 to tryptophan caused 5.5- or 46-fold decreases in affinity, respectively (Table 2). The double mutants followed a similar trend as in the USP10 assays with F15/33W and F33/124W having a more pronounced loss of affinity as compared to the individual single mutants. F15/124W only modestly reduced the affinity as compared to F15W, further suggesting that F124 does not contribute significantly to Caprin1 peptide binding, at least in the presence of F33. Unexpectedly, the TripleW mutant exhibited slightly increased affinity as compared to F15/33W. This discrepancy may be due to relatively poor solubility of the TripleW in the FP assay. As noted previously, our linear mixed-effects model confirms statistically significant, independent effects for F15W and F33W. On average, mutations caused relative decreases in affinity for Caprin1 ∼1 natural-log unit greater than for USP10 (p = 0.002), an effect that is particularly pronounced for the F33W substitution (p = 0.03).

Our FP assay results revealed that Caprin1 peptide binding was sensitive to mutation of residues F15 and F33. To determine the biological consequences of these mutations, we again overexpressed full-length His-tagged G3BP1 mutants in Expi293 cells and assayed for binding efficiency using the affinity capture copurification (Fig. 3*B*). With the exception of F124W, all mutants displayed a substantial deficiency in Caprin1 copurification, with reductions of ∼98% as compared to WT (Fig. 3*C*). Thus, in comparison to USP10, smaller fold changes in K_D values caused more dramatic changes in full-length G3BP1–Caprin1 complex stability (Fig. 2, orange), such that NTF2 domains with the same experimental 1:1 affinity for Caprin1 and USP10 systematically copurified ∼5-fold less Caprin1 (Fig. 2).

Sanders *et al.* (7) recently found a missense mutation in NTF2 (S38F), which blocks SG formation and is unable to form high affinity complexes with Caprin1. Unfortunately, NTF2 S38F expressed into insoluble inclusion bodies in *E. coli*. Mutations to Ala, Gly, or Thr were well tolerated, and we tested these mutants in USP10 and Caprin1 FP assays. As expected, all three mutants decreased the affinity for Caprin1 and at similar levels to F15W (Table 3). However, in the USP10 FP assay, NTF2 S38A or S38G increased affinity for USP10 by 2.9- or 2.4-fold, respectively, whereas S38T decreased affinity by 2.4-fold (Table 3). S38 is located on a loop away from the NTF2-binding groove, so these results suggest additional G3BP1 residues contribute to peptide binding. Additionally, the data further confirm prevailing hypotheses that small changes in affinities can cause significant changes in

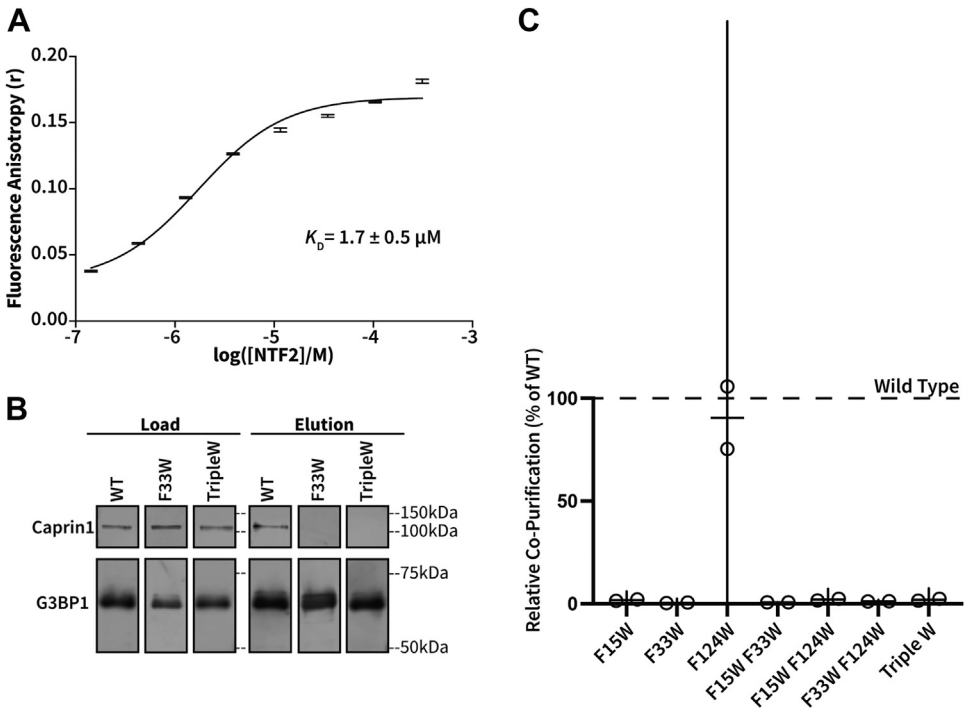

Figure 3. Individual equilibrium dissociation constants and copurification of G3BP1:Caprin1 interactions. *A*, an NTF2:Caprin1 binding isotherm was determined from fluorescence polarization assays. Fluorescence anisotropy data were collected, reported, and fit as described in Figure 1, using increasing concentrations of G3BP1 NTF2 in the presence of 30 nM reporter peptide derived from the Caprin1 binding motif (*F**-YNFIQDSMLDFE). Data represent the mean ± SD of n = 3 experiments. *B*, Expi293 cells were transfected with plasmids expressing His-G3BP1, WT or mutant, and lysates were subjected to affinity purification. Equal fractions of load (*left*) and eluates (*right*) were run on SDS-PAGE followed by immunoblotting with anti-G3BP1 (*bottom*) and anti-Caprin1 (*top*) antibodies. Both USP10 and Caprin1 copurify with G3BP1 in each experiment; as a result, the G3BP1 images here replicate the equivalent images in Figure 1*B*. *C*, immunoblots were analyzed *via* Image Studio and mutants were compared to WT. Data presented as individual values of n = 2 experiments and 95% confidence intervals (*vertical bars*).

protein–protein interactions in multivalent binding systems, such as transcription factors or viral receptors (47–49).

TripleW can cause significant conformational changes

Several crystal structures have been published of G3BP1 NTF2 in its apo form and complexed with peptides; however, no mutant crystal structures have been published. Given the dramatic reduction in complex formation as seen with the F33W and TripleW G3BP1 mutants, we wanted to determine the stereochemical cause of the defect. A crystal structure of G3BP1 NTF2 (1–139) TripleW was determined to a resolution of 2.36 Å. The structure was solved by molecular replacement using a deposited structure of G3BP1 NTF2 (Protein Data Bank [PDB] ID 4FCJ). The crystal structure is in space group $P\ 2_12_12_1$, with two molecules per asymmetric unit. The structure was refined to final R_{work} and R_{free} values of 22.2% and 27.1%, respectively, with excellent model geometry (Table 4).

The structure of G3BP1 NTF2 TripleW could be modeled from residues 1 to 138 except for loop residues 48 to 50 and 117 to 123 in chain B. Density for these loops is absent in other published apo crystal structures of G3BP1 NTF2 from the same space group. NTF2 TripleW dimerizes similarly to WT (PDB ID 4FCJ) and has no major changes in backbone conformations, with an all-atom calculated rmsd for the dimer of 0.57 Å (Fig. 4). When peptide-bound WT NTF2 dimers are compared to the apo WT NTF2 dimer, the calculated rmsd values are similarly small: 0.35 Å for the Caprin1 peptide (PDB ID 6TA7) and 0.46 Å for the FxFG peptide (PDB ID 4FCM).

The TripleW structure reveals major side-chain conformational changes in the binding groove compared to the WT structure (PDB ID 4FCJ). Residue 33 is dramatically twisted and shifted out of the groove when mutated to a tryptophan in chain A (Fig. 5, *A* and *C*). In chain B, W33 is similarly shifted out but with a smaller twist (Fig. 5, *B* and *D*). While the conformation adopted by W33 differs in chain A and chain B, both conformations are distinct from the WT F33 conformation (Fig. S4). Mutation of F33 to tryptophan appears to allow for greater flexibility in the side chain at residue 33, providing a potential albeit modest entropic advantage. The TripleW crystal structure demonstrates that W33 can adopt at least two

Table 2
Caprin1: G3BP1-NTF2 affinities

NTF2 construct	K_D (μM)
WT	1.7 ± 0.5
F15W	9.3 ± 1.7
F33W	79.3 ± 5.5
F124W	1.7 ± 0.4
F15/33W	256.1 ± 9.0
F15/124W	14.4 ± 4.0
F33/124W	133.0 ± 10
TripleW	240 ± 13

K_D values were estimated as described in Table 1 (see Fig. S3).

Table 3
Affinity of NTF2 S38 mutants for USP10 and Caprin1

Mutant	K_D (USP10) (μM)	K_D (Caprin1) (μM)
S38A	1.3 ± 0.3	7.3 ± 1.5
S38G	1.6 ± 0.3	10.5 ± 2.0
S38T	9.0 ± 0.4	11.8 ± 0.4

K_D values were estimated as described in Table 1 (see Figs. S2 and S3).

low energy conformations that are distinct from the WT F33 conformation. In chain A, the large conformational change in F33W causes it to occupy the steric volume that would normally be occupied by F13 from the USP10 FGDF motif peptide (Fig. 6*A*). F33W creates a similar residue level clash with I373 from the Caprin1 FIQDSMLD target sequence (Fig. 6*D*). In chain B, the conformational change in W33 does not create a steric clash with either the USP10 or Caprin1 peptide but W33 occupies a larger volume than the native phenylalanine (Fig. S5). Whichever of these conformation(s) may be found in solution, the binding data confirm that accommodation of the W33 side chain imposes a free energy cost on the binding of the peptides.

Mutations of F15W or F124W do not significantly alter the respective side-chain conformations, such that the mutant side chains overlay with the native side chains with steric differences confined to the difference in the size of the ring systems: replacement of phenylalanine with a tryptophan does increase the side-chain volume, which in turn shrinks the peptide-binding groove (Fig. 5, *C* and *D*). While F15W and F124W mutations cause changes in G3BP1 NTF2, they are much less dramatic than the changes associated with F33W. These differences likely explain why F33W has the most detrimental effect on binding affinity and complex formation.

Table 4
Crystal structure statistics

Data collection & reduction	
Beamline	NSLS-II 17-ID-1
Wavelength (Å)	0.92011
Space Group	$P\ 2_12_12_1$
Unit cell parameters:	
a, *b*, *c* (Å)	42.65, 71.67, 87.73
α, β, γ (°)	90, 90, 90
Resolution[a] (Å)	19.91–2.36 (2.5–2.36)
R_{meas}[b] (%)	36.6 (231.4)
$CC_{1/2}$[c] (%)	99.1 (34.9)
I/σ_I	7.02 (1.03)
Completeness	99.7 (99.9)
Redundancy	6.4 (6.0)
Refinement	
Total number of reflections	11,543 (1793)
Reflections in the test set	580
R_{work}[d]/R_{free}[e] (%)	22.2/27.1
Number of atoms:	
Protein	2204
Water	17
Ramachandran plot[f] (%)	95.75/4.25/0
RMSD bond length (Å)	0.01
RMSD bond angle ()	1.07
PDB ID	7S17

[a] Values in parentheses correspond to the highest resolution shell.
[b] R_{meas}: the redundancy independent R-factor, described in Diederichs and Karplus (1997); Nat. Struct. Biol. 4, 269–275.
[c] $CC_{½}$: the percentage of correlation between intensities from random half-datasets, described in detail in Karplus and Diederichs (2012); Science 336, 1030–1033.
[d] $R_{work} = \Sigma h\ |F_{obs}(h) - F_{calc}(h)|/\Sigma h F_{obs}(h)$, $h \in$ {working set}.
[e] $R_{free} = \Sigma h\ |F_{obs}(h) - F_{calc}(h)|/\Sigma h F_{obs}(h)$, $h \in$ {test set}.
[f] Favored/allowed/outliers.

Mutations in USP10 FGDF motif affect G3BP1 binding

Having identified key residues in the G3BP1 NTF2-binding groove responsible for binding USP10 and Caprin1 peptides, we turned to investigating residues in USP10 and Caprin1 that influence G3BP1 binding. While a previous group published an alanine scan in an FGDF-containing nsP3 peptide (32), there has yet to be a full amino-acid substitution analysis of the proposed FGDF or FIQDSMLD core motifs. We designed a peptide array in which the residues in the core motifs are individually substituted with all 20 genetically encoded amino acids. In the USP10 microarray (Fig. 7*A*), we chose to extend our analysis beyond the core motif to include three additional residues on the N- and C-terminal sides of the motif, so we scanned through the residues of a QYI**FGDF**SPD reference peptide. We performed the peptide array experiment at a protein concentration of 500 nM (∼9.1 μg/ml) of NTF2 protein; visualization of the amount of bound protein by antibody staining yielded variable spot intensities (Fig. 7*A*). As expected, the core FGDF motif contributes most of the binding specificity: most substitutions in these four amino acids reduced or abrogated G3BP1 NTF2 binding. The glycine residue (G11) is the most stringent requirement of the core motif, since all substitutions, except for alanine, dramatically reduce binding. The first phenylalanine residue (F10) tolerates tyrosine substitution and to a much lesser extent, valine, leucine, and isoleucine. The second phenylalanine (F13) tolerates substitution to tyrosine, valine, leucine, and isoleucine better than F10 and can accommodate a tryptophan. The aspartic acid (D12) is the least strict of the core motif residues because it can be mutated to most amino acids without dramatic changes in binding ability. The three upstream and downstream residues appear to have only modest and variable effects on G3BP1 NTF2 binding. Most mutations in these residues do not have dramatic changes in binding ability, although there may be some opportunities to enhance affinity by concerted tuning of these peripheral residues, as we have shown in the context of PDZ domains (50, 51).

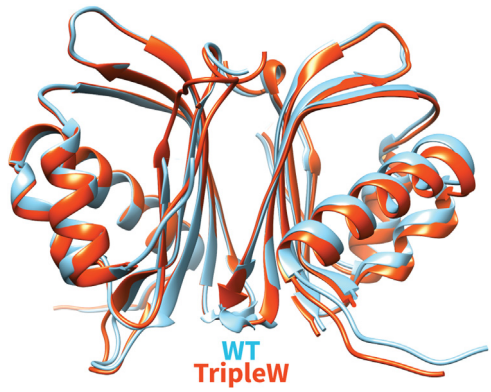

Figure 4. Structural conservation of the TripleW mutation. A cartoon representation of human G3BP1 NTF2-like domain TripleW (*rust*) is shown superimposed on G3BP1 NTF2-like domain WT (*sky blue*) (PDB ID 4FCJ), with all-atom calculated rmsd of 0.57 Å. PDB, Protein Data Bank.

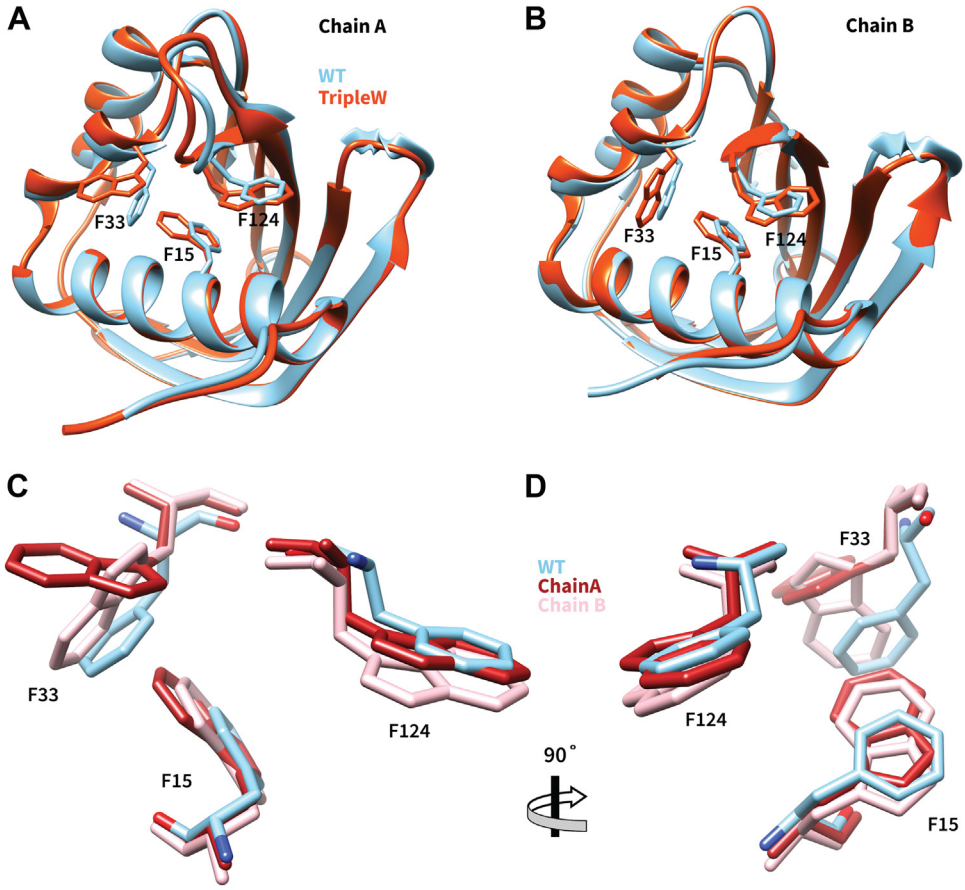

Figure 5. Stereochemical effects of Trp mutations in the NTF2 binding cleft. Cartoon representations of G3BP1 NTF2 chain A (*A*) and chain B (*B*) are shown, with TripleW (*rust*) superimposed onto WT (*sky blue*) (PDB ID 4FCJ). *C* and *D*, close-up stick figure models show the three phenylalanine residues that are mutated to tryptophan in the TripleW structure. TripleW Chain A: *red*, TripleW Chain B: *pink*, WT Chain A: *sky blue*. PDB, Protein Data Bank.

Caprin1 has multiple residue interactions with G3BP1

In the Caprin1 peptide array, we extended our amino-acid scan to include two additional residues on the N- and C-terminal sides of the previously reported core motif yielding YN**FIQDSMLD**FE as the reference sequence (28). Since our Caprin1 reporter peptide has a higher baseline affinity for G3BP1 NTF2 as calculated by FP, we incubated this array with 300 nM (∼5.5 μg/ml) of recombinant G3BP1 NTF2 (Fig. 7*B*). The phenylalanine residue at the N terminus of the core motif (F372) appears to be the most stringent residue in the core motif, since all substitutions completely abrogated binding to G3BP1 NTF2 (Fig. 7*B*). Substitutions at other positions were also disruptive, as expected. Surprisingly, we also found substitutions in the core motif that resulted in higher affinity peptides. For example, both I373F and S376C exhibited dramatic increases in the amount of bound G3BP1 NTF2. Additionally, replacements of M377 with phenylalanine or tyrosine each increased binding. The conserved core motif reported by Solomon *et al.* (28) had flexibility in three residues: F(M/**I**/L)Q(**D**/E)Sz(I/**L**)D. I373 substitution by leucine modestly increased affinity, where a methionine at this position ablated binding. Substitutions at the other two residues D375E and L378I modestly reduced binding. Surprisingly, Y370, which lies outside of the earlier core motif, appears to play an important role in binding: at this position all amino acids except for phenylalanine dramatically reduce binding. This suggests that the Caprin1 motif should be extended to include the residue Y370. Consistent with this proposal, mutation of N371 to alanine, glycine, or proline completely ablated binding, suggesting that it also lies within the binding motif. However, all other substitutions were well tolerated and some substitutions (Ile, Leu, Phe, and Trp) created higher affinity peptides. Substitutions of C-terminal flanking residues F380 and E381 were well tolerated and often produced higher affinity spots. Consistent with these results and in contrast to USP10, trimming of these motif flanking residues also created lower affinity peptides (Fig. S6). These data suggest that G3BP1 NTF2 interacts with more residues when binding Caprin1 than when binding USP10, which may account for the differential affinity we observed.

Additionally, we analyzed another reported G3BP1 interaction partner, USP13, which like USP10 has also been implicated in the postmaturational stability of CFTR (52, 53). The USP13-binding motif has not been previously reported, so we performed a scan of the N-terminal disordered region of the protein using overlapping 22mer peptides. Multiple spots contained peptides that appeared to interact with G3BP1 NTF2 (Fig. S7), including the N terminus, as well as a cluster

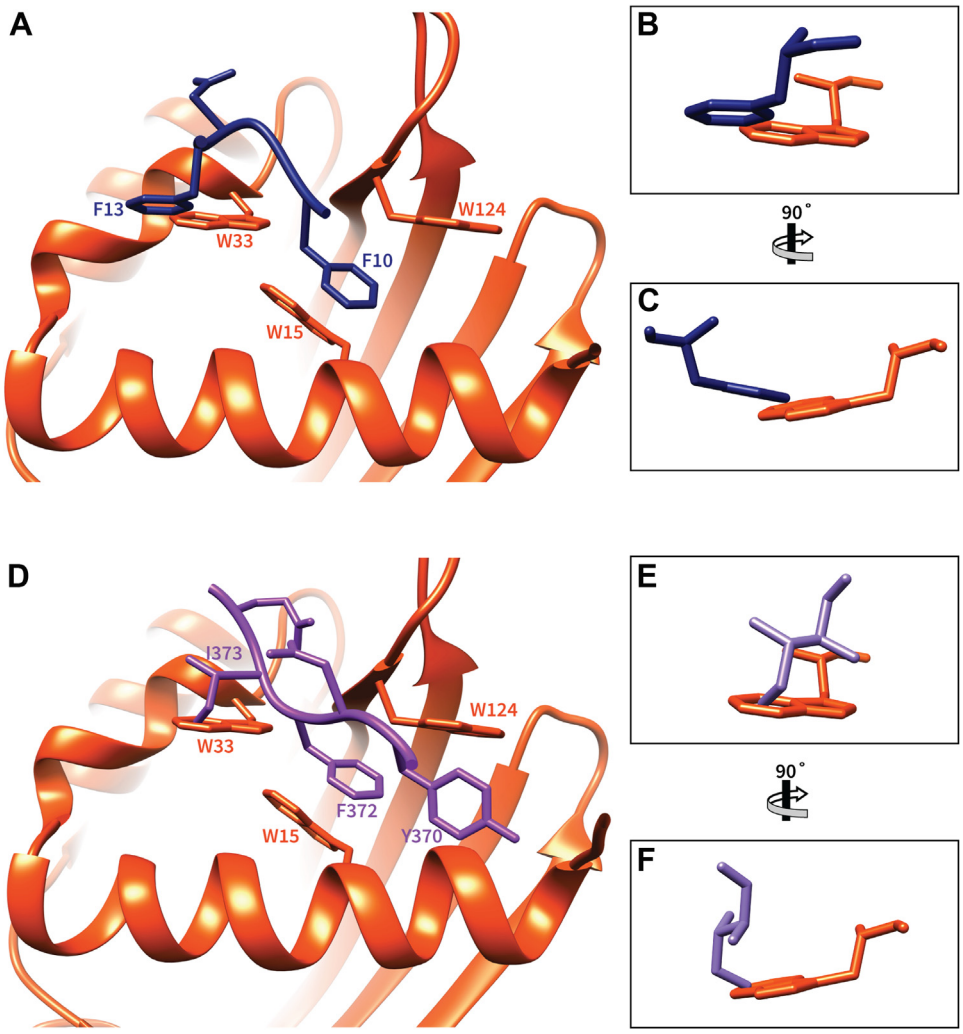

Figure 6. Impact of G3BP1 F33W mutation on USP10 and Caprin1 peptide binding. A cartoon representation of G3BP1 NTF2 TripleW is shown superimposed with the FGDF (*A*) and YNFIQD peptides (*D*) from the corresponding WT structures. The NTF2 TripleW structure was aligned with G3BP1 NTF2 WT cocrystal structures and then the WT NTF2 domain was omitted from the figure. *B* and *C*, isolated orthogonal views of the side-chain clash between G3BP1 NTF2 W33 (*rust*) and USP10 F13 (*navy*). *E* and *F*, isolated orthogonal views of the side-chain clash between G3BP1 NTF2 W33 (*rust*) and Caprin1 I373 (*purple*). The following cocrystal structures were used: (*A–C*) cocrystal structure of G3BP1 NTF2 WT with USP10 FGDF motif peptide (PDB ID 5DRV), (*D–F*) cocrystal structure of G3BP1 NTF2 WT with Caprin1 YNFIQD motif peptide (PDB ID 6TA7). PDB, Protein Data Bank.

involving peptides spanning amino acids 73 to 118. These data suggest that USP13 might have a relatively long motif peptide similar to Caprin1, or alternatively, that multiple motifs might be present within USP13. Further investigations will be needed to definitively identify the USP13-binding motif(s).

Discussion

In this work, we performed a thorough mutational analysis of the generative interactions that form G3BP1–USP10 and G3BP1–Caprin1 complexes. Using the smallest necessary components for these protein–protein interactions, the G3BP1 NTF2 domain and a motif peptide, we determined the binding affinities for multiple mutants ranging across a spectrum of two orders of magnitude and showed in copurification experiments that these affinities likely govern the stability of intermolecular assemblies involving G3BP1, USP10, and Caprin1. The effects of G3BP1 mutations on the affinities and stabilities of complexes formed with USP10 and Caprin1 are different and support the hypothesis that Caprin1 is more sensitive to disruption by mutagenesis than USP10, despite its higher baseline affinity. These results are consistent with other reports, in which relatively modest differences in protein:peptide interaction affinities have been associated with significant differences in the assembly of protein complexes. For example, the Ki-67 and RepoMan phosphatase regulatory proteins exhibit strong selectivity for protein phosphatase 1 (PP1) γ isoform over the α isoform, based on a roughly 4- to 6-fold difference in K_D arising primarily from a single amino acid difference (54).

Copurification has classically been used in nonaffinity chromatography schemes to purify tagless proteins from cells (55, 56). Proteins copurified using these schemes do not necessarily interact or form complexes directly, so additional experiments were necessary to prove protein–protein interactions. In our case, the direct interaction has already been

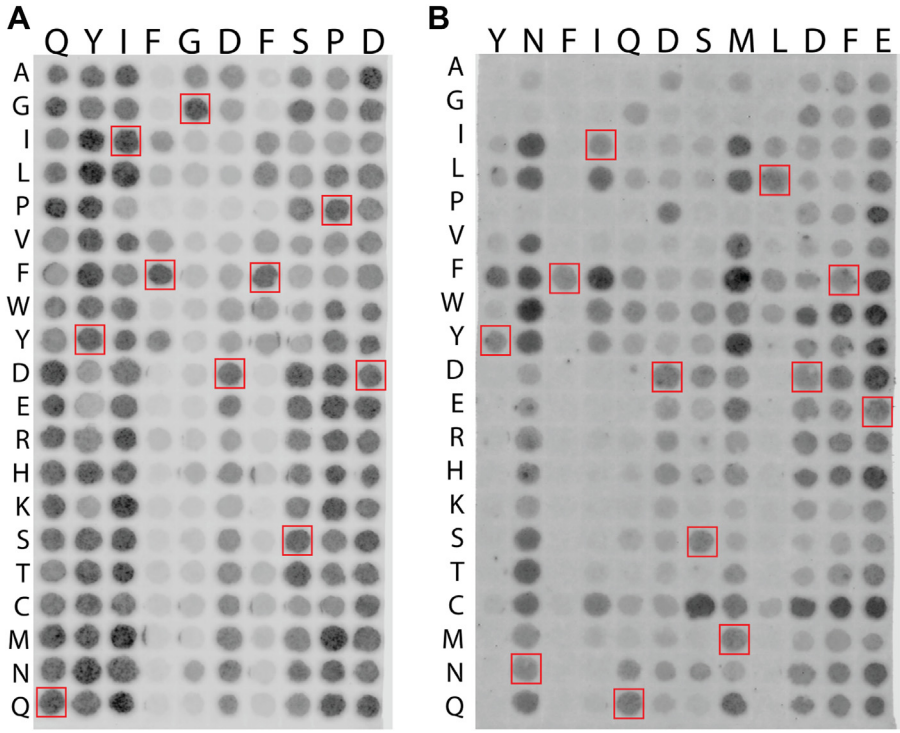

Figure 7. Binding of G3BP1 NTF2 to substituted USP10 and Caprin1 peptides. *A*, peptide cellulose SPOT array with single amino-acid substitutions in the USP10-binding peptide. Each spot contains the native USP10 peptide (HSP**QYIFGDFSPD**EFNQFFV) with a single amino acid in the native sequence (shown in the *top row* for *bold* residues in sequence) being replaced by the specific amino acid described by the amino acid code in the left column. *B*, peptide cellulose SPOT array with single amino acid substitutions in the Caprin1-binding peptide. Each spot contains the native Caprin1 peptide (QGP**YNFIQDSMLDFE**NQTLD) with a single amino acid in the native sequence (shown in the *top row* for *bold* residues in sequence) being replaced by the specific amino acid described by the amino acid code in the *left column*. *Red boxes* highlight peptides that match the native sequence. Darkness represents bound G3PB1 NTF2 protein as detected *via* antibody staining protocol.

established biochemically and crystallographically using purified components. Recent reports, however, have shown the benefits of affinity chromatography in copurifying protein complexes such as antibody stabilized proteins, RNA–protein complexes, and cytochrome supercomplex (57–59). The homogeneity of these purified complexes has been confirmed by biophysical methods such as small-angle X-ray scattering and protein crystallography (8, 57). G3BP1, USP10, and Caprin1 form protein complexes that are present within SGs that participate in liquid-liquid phase separation (7–9). Several reports have detailed the fluidity and reversibility of SGs (7–9); however, the G3BP1 complexes persisted through a strenuous purification scheme. This suggests that while the larger SG bodies may be fluid, the protein complexes within them may be unexpectedly persistent. Purification of protein complexes *via* metal affinity allows us to study them *in vitro* without the need to reconstitute the complex using recombinant versions of each individual component. And while not reported here, these purified protein complexes have been useful in development of additional assays. Given the complexity of our system, it was beneficial to use affinity copurification rather than the more common coimmunoprecipitation. While we report our copurification data as in terms of percentage of WT recovery, we are effectively measuring the off-rate of these protein–protein interactions, which appears to be very slow, consistent with multivalency of the SGs. The data reported here provide additional evidence that affinity copurification is a useful tool for *in vitro* investigations of large proteins complexes.

Based on prior data, we were somewhat surprised by the results of the FP assay and copurification experiments using the F15W mutant. In the FP assays, G3BP1 NTF2 F15W had calculated K_D values of 11.6 μM and 9.3 μM for USP10 and Caprin1, respectively. These values are similar and are each less than one order of magnitude different from WT, so we expected reduced, but not abolished, USP10 and Caprin1 copurification. Indeed, the longer Caprin1 binding motif (FIQDSMLD) might have been expected to be more stable to disruption by a single amino acid substitution. However, the opposite result was observed. While USP10 copurification was reduced by ∼50% compared to WT, the G3BP1 F15W mutation almost entirely abolished Caprin1 copurification.

One possible explanation is that the off-rate of the larger Caprin1 binding peptide may be faster, even if the affinity is similar. Previous crystal structures have demonstrated the importance of hydrophobic interactions and π-stacking in the G3BP1 groove for USP10 and Caprin1 peptide binding (17, 26, 30). As a result, this disjunction between USP10 and Caprin1 binding may well reflect differences in the motif peptides, since the USP10 FGDF motif contains two phenylalanines, whereas the Caprin1 FIQDSMLD motif contains only one. G3BP1 F15 participates in parallel-displaced π-stacking with USP10 F10 and Caprin1 F372. When mutated to a tryptophan, residue 33 occupies a larger hydrophobic volume with a slightly adjusted

side chain (Fig. 5). This change sterically occludes the positioning the USP10 and Caprin1 peptides (Fig. 6), most likely accounting for the observed reduction in affinity. The impact on the USP10 off-rate may be less dramatic, since it has a second phenylalanine, F13, that can still form π-stacking interactions with G3BP1 F33. During binding, USP10 F10 and Caprin1 I373 occupy the same position in the G3BP1-binding groove. Interestingly, in the Caprin1 microarray experiment, I373F created a higher affinity peptide. Thus, is it possible that Caprin1 I373F could rescue Caprin1 copurification in the G3BP1 F15W overexpression system.

The literature describing G3BP1–USP10 and G3BP1–Caprin1 complexes has primarily focused on mutational and functional analyses of G3BP1 residues and binding interfaces (7–9, 29, 30). We also wanted to understand the contributions from USP10 and Caprin1 in complex formation. Using a systematic amino acid scan, we have confirmed that the USP10 FGDF motif is the smallest necessary component for G3BP1 NTF2 binding (32). As expected, most substitutions in the core FGDF motif created lower affinity peptides, while substitutions in the upstream and downstream residues modulated affinity but were mostly well tolerated (Fig. 7*A*). In particular, substitution of flanking residues Y8 and I9 has the potential to create higher affinity peptides.

In the Caprin1 array, we saw that most substitutions in the FIQDSMLD motif created lower affinity peptides (Fig. 7*B*), again confirming the importance of the previously reported motif (28). However, substitutions I373F, S376C, M377F, and M377Y created higher affinity peptides. Given that I373 sits similarly to USP10 F13, it is unsurprisingly that replacement with a phenylalanine creates a higher affinity peptide. Similar to the USP10 peptide array, upstream and downstream amino acid substitutions often created higher affinity peptides; however, flanking residues have a greater role in Caprin1 binding (Fig. S6). In particular, Y370 appears to play a critical role in G3BP1 binding since it only tolerated substitution to phenylalanine (Fig. 7*B*), and binding was abolished when it was removed (Fig. S6).

The ability of the NTF2-binding site to accommodate stereochemical changes in binding partners may mirror the (limited) flexibility seen in the TripleW structure. Despite the presence of three mutant sidechain with increased steric bulk in the binding cleft, different conformations are observed for W33 in monomers A and B (Fig. 5). Furthermore, modeling of the peptide–NTF2 complexes (Fig. 6) suggests that the peptides are not deeply buried in the cleft, but rather interact at the surface, in a way that can facilitate alternative stereochemical engagement of mutant residues. The observed binding data may provide a useful foundation for future modeling studies.

G3BP1–USP10 and G3BP1–Caprin1 complex formation are associated with the progression of several diseases (60–63). For example, the COSMIC database revealed that mutations in G3BP1, USP10, and Caprin1 occur in less than 5% of cancers; however, gene expression was more varied, with all three proteins showing overexpression and underexpression in several cancer types (64). It may ultimately prove therapeutically useful to target one or both component interactions selectively. Given that the necessary component for complex formation is NTF2 and short motif peptides, we could easily adapt our FP assay to perform high throughput screens for novel inhibitors. Data from our peptide array studies could also be used to generate higher affinity peptides that would be necessary for the screening of novel inhibitors. Indeed, we have previously shown in a separate protein–peptide interaction that our medium throughput FP assay is easily translated to high throughput screening studies (65).

Currently, there are two published G3BP1 targeted peptide therapies including GAP161 (22), which blocks RasGAP association, and GAP159 (66), which inhibits G3BP1 expression. Resveratrol, an anticancer agent, has been shown to bind the G3BP1 NTF2-like domain and induce apoptosis *via* p53 activation (31, 67). While these therapies are targeted toward cancer progression and metastasis, they do support the concept of targeting G3BP1 and its complex formation as advantageous and novel drug targets.

Benefits arising from the ability to inhibit or control G3BP1 complex formation are observed in nature as well. During viral attack, infected cells will activate stress granule formation to block mRNA processing and halt viral growth (68). As an essential component of SGs, G3BP1 plays an important role in the antiviral response. Viruses use the FGDF-containing nsP3 to bind G3BP1 and sequester it away from stress granules, thereby inhibiting stress granule formation and allowing viral growth (17). G3BP1 NTF2-like domain has been reported to interact with the nsP3 protein from many viruses including SARS-CoV-2, Old World alphavirus, Semliki Forest virus, Sindbis virus, Herpes Simplex virus, and chikungunya (24, 32, 69–73).

Finally, USP10 is a deubiquitinase that plays an important role in protein homeostasis and recycling. One target of USP10 is CFTR, a chloride channel that helps maintain ion balance across epithelial cells in the lungs and other tissues (36). As part of its normal lifecycle, CFTR is retrieved from the plasma membrane into endosomes for peripheral quality control (74). USP10 deubiquitinates CFTR in endosomes, thereby increasing the probability of endocytic recycling, which in turn helps to maintain the abundance of CFTR at the plasma membrane. In lung infections caused by *Pseudomonas aeruginosa*, a virulence factor called Cif is secreted from the bacteria in outer membrane vesicles and is able to trigger a reduction in plasma membrane CFTR levels (20, 75). Cif stabilizes a G3BP1–USP10 complex in lung cells, which renders USP10 inactive and thus unable to deubiquitinate CFTR (20, 36, 75). Knockdown of G3BP1 blocks the Cif effect, suggesting that USP10 expression and activity is protective for CFTR and ion homeostasis during *P. aeruginosa* infections (20). Thus, while it is not known how Cif drives G3BP1–USP10 complex formation, inhibitors of the interaction could also help to neutralize Cif-facilitated CFTR degradation.

The data reported here will facilitate future experiments on the roles of G3BP1, USP10, and Caprin1. We have identified

several mutations in the three proteins that alter binding affinity by large and small amounts. As we have shown, small changes in affinity can have dramatic effects on the cell biology of the system, so we can use these mutations to selectively manipulate the G3BP1-USP10-Caprin1 system. This will help deconvolute the intricate interaction network surrounding these three proteins and help address unanswered questions in disease contexts including bacterial virulence, antiviral response, innate immunity, and neurodegeneration.

Experimental procedures

Cloning, protein expression, and purification

The pNIC28-G3BP1-NTF2 vector was graciously provided by Dr Gerald McInerney (Karolinska Institutet, Stockholm, Sweden). The vector contained the sequence of the NTF2-like domain (amino acids 1–139) of human G3BP1 (UniProt ID Q13283). Mutants were created *via* site-directed mutagenesis using primers designed on NEBaseChanger and Q5 site-directed mutagenesis kit following manufacturer's directions (New England BioLabs). BL21(DE3) cells were transformed with plasmid and grown on LB (76) + 50 μg/ml kanamycin agar plates at 37 °C overnight. Transformants were used to inoculate 10 ml LB + 50 μg/ml kanamycin broth and grown at 37 °C overnight. Overnight cultures were used to inoculate 1 l LB + 50 μg/ml kanamycin broth in nonbaffled 2 l flasks and allowed to grow at 37 °C with shaking. Once the A_{600} of the cultures reached ∼0.8, the cultures were induced with 0.1 mM IPTG and transferred to 30 °C with shaking for 4 h. Cultures with mutant G3BP1 NTF2 were expressed at 16 °C with shaking overnight (∼18 h). After expression, cultures were pelleted in a JLA-9.1000 rotor at 4500 rpm for 15 min at 4 °C. Pellet was resuspended in lysis buffer (500 mM NaCl, 20 mM Tris pH 8.5, 2 mM $MgCl_2$) supplemented with Pierce universal nuclease at 25 units/ml and Roche cOmplete EDTA-free protease inhibitor cocktail tablets. Cell lysis was carried out using an M-110L microfluidizer (Microfluidics) in three passes at ∼18 kpsi. Lysate was spun down for 1 h at 40K rpm at 4 °C in a Type 45 Ti rotor. Five milliliters of HisPur Ni-NTA Resin (Thermo Scientific) was washed with 25 ml wash buffer (500 mM NaCl, 20 mM Tris, pH 8.5). The clarified cell lysate was supplemented with 20 mM imidazole, pH 8.5, and then incubated with Ni-NTA resin with gentle stirring for 1 h at 4 °C. The mixture was returned to room temperature (RT) and passed through a gravity flow column. The protein-bound resin was washed four times with 25 ml of wash buffer supplemented with 80 mM imidazole, pH 8.5. The protein was eluted with 500 mM NaCl, 20 mM Tris pH 8.5, and 500 mM imidazole, pH 8.5. Eluates were immediately diluted 1:1 with 800 mM NaCl and 20 mM Tris, pH 8.5 then pooled for dialysis at RT into 500 mM NaCl and 20 mM Tris, pH 8.5. After at least an hour of dialysis, purified recombinant TEV was added at a ratio of 1:20 and left at RT overnight. The cleaved protein was passed through HisPur Ni-NTA resin equilibrated with wash buffer. The flow through was collected, concentrated, and loaded on a HiLoad 26/600 Superdex 200 pg size-exclusion chromatography column (GE Healthcare). Protein was eluted using a buffer of 150 mM NaCl and 20 mM Tris pH 8.5 at the expected molecular mass (Fig. S8).

Full-length human G3BP1 (UniProt ID Q13283) was expressed and purified from Expi293F cells (Life Tech) as detailed here. The pCMV-His-G3BP1 vector was purchased from SinoBiolgical. Mutants were generated using the same site-directed mutagenesis protocol as detailed previously. Expi293F cells were grown in Expi293 Expression Media at 37 °C, 8% CO_2 with shaking at 125 rpm in a disposable plastic Erlenmeyer flask (nonbaffled). On the day of transfection, cell density was between 4 to 5 × 10^6 cells/ml with >95% viability as determined using a TC20 automated cell counter (Bio-Rad). Cells were diluted with warm Expi293 Expression Media to 2 × 10^6 cells/ml in 42.5 ml. Five micrograms of plasmid was added to 2.5 ml Opti-MEM reduced-serum medium (Gibco). Fifteen micrograms of sterile PEI was added to 2.5 ml Opti-MEM reduced-serum medium. PEI solution was added to DNA solution, inverted several times, and incubated for 20 min at RT. DNA:PEI solution was added to the flask of Expi293 cells then returned to incubator at 37 °C, 8% CO_2 with shaking at 125 rpm. After 16 to 20 h, 25 μl of 100 mM sterile-filtered valproic acid (Sigma) and 2.5 ml of 100 mM sterile-filtered sodium propionate (Sigma) in Expi293TM Expression Medium were added to the flask. Seventy-two hours after transfection, cells were gently pelleted and then resuspended in lysis buffer (500 mM NaCl, 20 mM Tris pH 8.5, 1% [*v/v*] IGEPAL, 2 mM $MgCl_2$) supplemented with Pierce universal nuclease at 25 units/ml and Roche cOmplete EDTA-free protease inhibitor cocktail tablets. Conical tubes were placed on gentle rotator for 30 min at 4 °C. Clarification and elution followed the same protocol as aforementioned. After elution, samples from first eluate were collected, boiled in SDS sample buffer, and run on a 10% SDS acrylamide gel. Proteins were transferred to a polyvinylidene difluoride membrane at 95 V for 2 h at 4 °C. Membranes were blocked for 1 h at RT in Odyssey blocking buffer (LiCor). Primary antibodies (rabbit polyclonal USP10 antibody, Bethyl; rabbit polyclonal Caprin1 antibody, Proteintech; mouse monoclonal G3BP1 antibody, Santa Cruz) were diluted into Odyssey blocking buffer with 0.2% (*v/v*) Tween 20. Membranes were incubated with primary antibody solutions overnight at 4 °C. Membranes were washed with Tris-buffered saline, 0.1% (*v/v*) Tween 20 (TBST) then incubated for 1 h in IRDye secondary antibody (LiCor) in Odyssey blocking buffer with 0.2% (*v/v*) Tween 20 + 0.01% (*w/v*) SDS. Membranes were washed with TBST multiple times and then imaged with the Odyssey CLx Imager (LiCor).

FP

FP assays were performed following lab established protocols (77, 78). Briefly, experiments were performed using G3BP1 NTF2 protein and performed in triplicate. Biomatik synthesized the reporter peptides used for all FP experiments: fluorescein-aminohexanoic acid (*F**)-YIFGDFSP (USP10) and *F**-YNFIQDSMLDFE (Caprin1). All experiments were performed in stock buffer (150 mM NaCl, 20 mM Tris, pH 8.5) supplemented with 30 μM thesit and 0.1 mg/ml IgG. Protein

was serially diluted into stock buffer containing 30 nM reporter peptide then transferred to a 384-well plate. The protein-reporter mixture was allowed to incubate at RT for 30 min. Plates were scanned on a Synergy Neo2 multimode plate reader (BioTek), and anisotropy was measured with an excitation wavelength of 485 nm and an emission wavelength of 528 nm. Anisotropy and intensity values were analyzed manually to confirm no effect due to light scattering. A nonlinear least-squares single-site binding algorithm in Prism was used to fit the anisotropy data from three independent titrations, yielding estimates for the K_D and SD.

Crystallography

G3BP1 NTF2 TripleW crystals were obtained by vapor diffusion in a sitting drop composed of 200 nl of 1.6 mg/ml protein in 100 mM NaCl, 20 mM Tris, pH 8.5, and 200 nl of well solution (20% [*w/v*] PEG 8000, 100 mM HEPES pH 7.5) and equilibrated by vapor diffusion with 50 µl of well solution. The drop was set up using a NT8 drop setter (Formulatrix) and the well solution was from the Wizard Classic I&II High-Throughput Screen (Molecular Dimensions). The tray was incubated and imaged using Rock Imager and Rock Maker instrumentation (Formulatrix). The crystal was harvested straight from the screening drop without cryoprotectant or oil and immediately flash cooled in liquid nitrogen. The rotation data collection was performed at the National Synchrotron Light Source II beamline 17-ID-2 (FMX) equipped with an Eiger 16M detector at 100 K, a rotation range of 0.2° per frame, and a total of wedge of 180°. The diffraction images were processed using XDS (79). The R_{free} set was generated from 5% of the reflections in thin resolution shells using the Phenix (80) reflection file editor. Initial phases were generated by Phaser (81) *via* molecular replacement using G3BP1 NTF2 WT (PDB ID 4FCJ) as a search model. Iterative automatic and manual refinement was performed using Phenix and Coot (80, 82).

Peptide array

The 600 peptide SPOT cellulose array was generated by the Biopolymers & Proteomics Core Facility at the Koch Institute for Integrative Cancer Research of Massachusetts Institute of Technology. An Intavis SPOT synthesis peptide arrayer system was used to make the array.

The peptide array was hydrated with methanol for 10 min, then washed three times with TBST, and then blocked for 2 h in Odyssey blocking buffer. The array was incubated with His-tagged G3BP1 NTF2 in blocking buffer with 0.2% (*v/v*) Tween 20 for ∼20 h at 4 °C and then washed three times with TBST. G3BP1 was detected using a His-tag antibody (Santa Cruz) followed by IRDye secondary antibody in Odyssey blocking buffer with 0.2% (*v/v*) Tween 20 + 0.01% (*w/v*) SDS. Arrays were scanned on an Odyssey CLx Imager.

Statistical models of mutation and ligand effects

Linear models were used to estimate the impact of mutation on binding affinity and coprecipitation. Random effects due to different Western blots were accounted for using mixed effects linear models in the R programming environment using nlme (83). Our statistical models included binary (yes/no) variables for each mutation (F15, F33, F124) and relevant ligand (G3BP1, USP10, Caprin1). Possible interactions between mutations were tested as well as interactions between ligands and mutations. Figure 2 was generated using ggplot2 (84).

Data availability

The coordinates and structure factors for the G3BP1 NTF2-like domain TripleW structure are available at the Protein Data Bank under PDB ID: 7S17. All other data described are contained within this article.

Supporting information—This article contains supporting information.

Acknowledgments—We would like to thank Drs Babak Andi, Martin Fuchs, Alexei Soares, and Vivian Stojanoff at the NSLS-II MX beamlines for support of diffraction experiments, Dr Noor Taher for advice and suggestions regarding data processing and structure refinement, Dr Kelli Hvorecny for mentorship and advice, Dr Andreia Verissimo and Dr Angela Kull for the support of the bioMT core facilities, Dr Bradley Bartholomai and members of the Madden and Stanton lab for helpful discussions.

Author contributions—C. T. S. and D. R. M. conceptualization; C. T. S. and D. R. M. methodology; C. T. S. and T. H. H. validation; C. T. S. and T. H. H. formal analysis; C. T. S. investigation; C. T. S. writing–original draft; C. T. S., T. H. H., and D. R. M. writing–review & editing; C. T. S. and T. H. H. visualization; D. R. M. project administration; D. R. M. funding acquisition.

Funding and additional information—This work was supported by National Institutes of Health grants R01-AI091699, P20-GM113132, and P30-DK117469, training grant T32-HL134598, and beamline support P30-GM133893. Additional beamline funding was provided by US Department of Energy contracts DE-SC0012704 and KP1607011. The content is solely the responsibility of the authors and does not necessarily represent the official views of the National Institutes of Health or the US Department of Energy.

Conflict of interest—The authors declare that they have no conflicts of interest with the contents of this article.

Abbreviations—The abbreviations used are: Caprin1, cytoplasmic activating/proliferation associated protein 1; CFTR, cystic fibrosis transmembrane conductance regulator; DUB, deubiquitinating enzyme; FP, fluorescence polarization; G3BP1, Ras GTPase activating protein SH3 domain binding protein 1; IDP, intrinsically disordered protein; NTF2, nuclear transport factor 2-like domain; PDB, Protein Data Bank; SG, stress granule; USP10, ubiquitin-specific peptidase 10.

References

1. Dunker, A. K., Cortese, M. S., Romero, P., Iakoucheva, L. M., and Uversky, V. N. (2005) Flexible nets. The roles of intrinsic disorder in protein interaction networks. *FEBS J.* **272**, 5129–5148

2. Kim, P. M., Sboner, A., Xia, Y., and Gerstein, M. (2008) The role of disorder in interaction networks: a structural analysis. *Mol. Syst. Biol.* **4**, 179
3. Wright, P. E., and Dyson, H. J. (2015) Intrinsically disordered proteins in cellular signaling and regulation. *Nat. Rev. Mol. Cell Biol.* **16**, 18–29
4. Wright, P. E., and Dyson, H. J. (1999) Intrinsically unstructured proteins: re-assessing the protein structure-function paradigm. *J. Mol. Biol.* **293**, 321–331
5. Dyson, H. J., and Wright, P. E. (2005) Intrinsically unstructured proteins and their functions. *Nat. Rev. Mol. Cell Biol.* **6**, 197–208
6. Oldfield, C. J., Cheng, Y., Cortese, M. S., Romero, P., Uversky, V. N., and Dunker, A. K. (2005) Coupled folding and binding with α-helix-forming molecular recognition elements. *Biochemistry* **44**, 12454–12470
7. Sanders, D. W., Kedersha, N., Lee, D. S. W., Strom, A. R., Drake, V., Riback, J. A., *et al.* (2020) Competing protein-RNA interaction networks control multiphase intracellular organization. *Cell* **181**, 306–324.e28
8. Yang, P., Mathieu, C., Kolaitis, R.-M., Zhang, P., Messing, J., Yurtsever, U., *et al.* (2020) G3BP1 is a tunable switch that triggers phase separation to assemble stress granules. *Cell* **181**, 325–345.e28
9. Guillén-Boixet, J., Kopach, A., Holehouse, A. S., Wittmann, S., Jahnel, M., Schlüßler, R., *et al.* (2020) RNA-induced conformational switching and clustering of G3BP drive stress granule assembly by condensation. *Cell* **181**, 346–361.e17
10. Parker, F., Maurier, F., Delumeau, I., Duchesne, M., Faucher, D., Debussche, L., *et al.* (1996) A Ras-GTPase-activating protein SH3-domain-binding protein. *Mol. Cell. Biol.* **16**, 2561–2569
11. Gallouzi, I. E., Parker, F., Chebli, K., Maurier, F., Labourier, E., Barlat, I., *et al.* (1998) A novel phosphorylation-dependent RNase activity of GAP-SH3 binding protein: a potential link between signal transduction and RNA stability. *Mol. Cell. Biol.* **18**, 3956–3965
12. Tourrière, H., Gallouzi, I. E., Chebli, K., Capony, J. P., Mouaikel, J., van der Geer, P., *et al.* (2001) RasGAP-associated endoribonuclease G3Bp: selective RNA degradation and phosphorylation-dependent localization. *Mol. Cell. Biol.* **21**, 7747–7760
13. Tourrière, H., Chebli, K., Zekri, L., Courselaud, B., Blanchard, J. M., Bertrand, E., *et al.* (2003) The RasGAP-associated endoribonuclease G3BP assembles stress granules. *J. Cell Biol.* **160**, 823–831
14. Prigent, M., Barlat, I., Langen, H., and Dargemont, C. (2000) IκBα and IκBα/NF-κB complexes are retained in the cytoplasm through interaction with a novel partner, RasGAP SH3-binding protein 2. *J. Biol. Chem.* **275**, 36441–36449
15. Soncini, C., Berdo, I., and Draetta, G. (2001) Ras-GAP SH3 domain binding protein (G3BP) is a modulator of USP10, a novel human ubiquitin specific protease. *Oncogene* **20**, 3869–3879
16. Zekri, L., Chebli, K., Tourrière, H., Nielsen, F. C., Hansen, T. V. O., Rami, A., *et al.* (2005) Control of fetal growth and neonatal survival by the RasGAP-associated endoribonuclease G3BP. *Mol. Cell. Biol.* **25**, 8703–8716
17. Schulte, T., Liu, L., Panas, M. D., Thaa, B., Dickson, N., Götte, B., *et al.* (2016) Combined structural, biochemical and cellular evidence demonstrates that both FGDF motifs in alphavirus nsP3 are required for efficient replication. *Open Biol.* **6**, 160078
18. Irvine, K., Stirling, R., Hume, D., and Kennedy, D. (2004) Rasputin, more promiscuous than ever: a review of G3BP. *Int. J. Dev. Biol.* **48**, 1065–1077
19. Piatnitskaia, S., Takahashi, M., Kitaura, H., Katsuragi, Y., Kakihana, T., Zhang, L., *et al.* (2019) USP10 is a critical factor for tau-positive stress granule formation in neuronal cells. *Sci. Rep.* **9**, 10591
20. Bomberger, J. M., Ye, S., MacEachran, D. P., Koeppen, K., Barnaby, R. L., O'Toole, G. A., *et al.* (2011) A *Pseudomonas aeruginosa* toxin that hijacks the host ubiquitin proteolytic system. *PLoS Pathog.* **7**, e1001325
21. Li, Y., Wang, J., Zhong, S., Li, J., and Du, W. (2020) Overexpression of G3BP1 facilitates the progression of colon cancer by activating β-catenin signaling. *Mol. Med. Rep.* **22**, 4403–4411
22. Zhang, H., Zhang, S., He, H., Zhao, W., Chen, J., and Shao, R. (2012) GAP161 targets and downregulates G3BP to suppress cell growth and potentiate cisplaitin-mediated cytotoxicity to colon carcinoma HCT116 cells. *Cancer Sci.* **103**, 1848–1856
23. Zhang, H., Zhang, S. H., He, H. W., Zhang, C. X., Yu, D. K., and Shao, R. G. (2013) Downregulation of G3BPs inhibits the growth, migration and invasion of human lung carcinoma H1299 cells by suppressing the Src/FAK-associated signaling pathway. *Cancer Gene Ther.* **20**, 622–629
24. Alam, U., and Kennedy, D. (2019) Rasputin a decade on and more promiscuous than ever? A review of G3BPs. *Biochim. Biophys. Acta Mol. Cell Res.* **1866**, 360–370
25. Kennedy, D., French, J., Guitard, E., Ru, K., Tocque, B., and Mattick, J. (2001) Characterization of G3BPs: tissue specific expression, chromosomal localisation and rasGAP(120) binding studies. *J. Cell. Biochem.* **84**, 173–187
26. Kristensen, O. (2015) Crystal structure of the G3BP2 NTF2-like domain in complex with a canonical FGDF motif peptide. *Biochem. Biophys. Res. Commun.* **467**, 53–57
27. Vognsen, T., Møller, I. R., and Kristensen, O. (2013) Crystal structures of the human G3BP1 NTF2-like domain visualize FxFG Nup repeat specificity. *PLoS One* **8**, e80947
28. Solomon, S., Xu, Y., Wang, B., David, M. D., Schubert, P., Kennedy, D., *et al.* (2007) Distinct structural features of caprin-1 mediate its interaction with G3BP-1 and its induction of phosphorylation of eukaryotic translation initiation factor 2α, entry to cytoplasmic stress granules, and selective interaction with a subset of mRNAs. *Mol. Cell. Biol.* **27**, 2324–2342
29. Kedersha, N., Panas, M. D., Achorn, C. A., Lyons, S., Tisdale, S., Hickman, T., *et al.* (2016) G3BP-Caprin1-USP10 complexes mediate stress granule condensation and associate with 40S subunits. *J. Cell Biol.* **212**, 845–860
30. [preprint] Schulte, T., Panas, M. D., Williams, L., Kedersha, N., Fleck, J. S., Tan, T. J. C., *et al.* (2021) Caprin-1 binding to the critical stress granule protein G3BP1 is regulated by pH. *bioRxiv*. https://doi.org/10.1101/2021.02.05.429362
31. Oi, N., Yuan, J., Malakhova, M., Luo, K., Li, Y., Ryu, J., *et al.* (2015) Resveratrol induces apoptosis by directly targeting Ras-GTPase-activating protein SH3 domain-binding protein 1. *Oncogene* **34**, 2660–2671
32. Panas, M. D., Schulte, T., Thaa, B., Sandalova, T., Kedersha, N., Achour, A., *et al.* (2015) Viral and cellular proteins containing FGDF motifs bind G3BP to block stress granule formation. *PLoS Pathog.* **11**, e1004659
33. Yuan, J., Luo, K., Zhang, L., Cheville, J. C., and Lou, Z. (2010) USP10 regulates p53 localization and stability by deubiquitinating p53. *Cell* **140**, 384–396
34. Liu, J., Xia, H., Kim, M., Xu, L., Li, Y., Zhang, L., *et al.* (2011) Beclin1 controls the levels of p53 by regulating the deubiquitination activity of USP10 and USP13. *Cell* **147**, 223–234
35. Boulkroun, S., Ruffieux-Daidié, D., Vitagliano, J.-J., Poirot, O., Charles, R.-P., Lagnaz, D., *et al.* (2008) Vasopressin-inducible ubiquitin-specific protease 10 increases ENaC cell surface expression by deubiquitylating and stabilizing sorting nexin 3. *Am. J. Physiol. Renal Physiol.* **295**, F889–F900
36. Bomberger, J. M., Barnaby, R. L., and Stanton, B. A. (2009) The deubiquitinating enzyme USP10 regulates the post-endocytic sorting of cystic fibrosis transmembrane conductance regulator in airway epithelial cells. *J. Biol. Chem.* **284**, 18778–18789
37. Lin, Z., Yang, H., Tan, C., Li, J., Liu, Z., Quan, Q., *et al.* (2013) USP10 antagonizes c-Myc transcriptional activation through SIRT6 stabilization to suppress tumor formation. *Cell Rep.* **5**, 1639–1649
38. Grunda, J. M., Nabors, L. B., Palmer, C. A., Chhieng, D. C., Steg, A., Mikkelsen, T., *et al.* (2006) Increased expression of thymidylate synthetase (TS), ubiquitin specific protease 10 (USP10) and survivin is associated with poor survival in glioblastoma multiforme (GBM). *J. Neurooncol.* **80**, 261–274
39. Weisberg, E. L., Schauer, N. J., Yang, J., Lamberto, I., Doherty, L., Bhatt, S., *et al.* (2017) Inhibition of USP10 induces degradation of oncogenic FLT3. *Nat. Chem. Biol.* **13**, 1207–1215
40. Takahashi, M., Kitaura, H., Kakita, A., Kakihana, T., Katsuragi, Y., Nameta, M., *et al.* (2018) USP10 is a driver of ubiquitinated protein aggregation and aggresome formation to inhibit apoptosis. *iScience* **9**, 433–450
41. Wang, B., David, M. D., and Schrader, J. W. (2005) Absence of caprin-1 results in defects in cellular proliferation. *J. Immunol.* **175**, 4274–4282

42. Qiu, Y.-Q., Yang, C.-W., Lee, Y.-Z., Yang, R.-B., Lee, C.-H., Hsu, H.-Y., *et al.* (2015) Targeting a ribonucleoprotein complex containing the caprin-1 protein and the c-Myc mRNA suppresses tumor growth in mice: an identification of a novel oncotarget. *Oncotarget* **6**, 2148–2163
43. El Fatimy, R., Tremblay, S., Dury, A. Y., Solomon, S., De Koninck, P., Schrader, J. W., *et al.* (2012) Fragile X mental retardation protein interacts with the RNA-binding protein Caprin1 in neuronal RiboNucleoProtein complexes. *PLoS One* **7**, e39338
44. Yang, Z.-S., Qing, H., Gui, H., Luo, J., Dai, L.-J., and Wang, B. (2019) Role of caprin-1 in carcinogenesis. *Oncol. Lett.* **18**, 15–21
45. Bhattacharya, U., Neizer-Ashun, F., Mukherjee, P., and Bhattacharya, R. (2020) When the chains do not break: the role of USP10 in physiology and pathology. *Cell Death Dis.* **11**, 1033
46. Kim, T. H., Tsang, B., Vernon, R. M., Sonenberg, N., Kay, L. E., and Forman-Kay, J. D. (2019) Phospho-dependent phase separation of FMRP and CAPRIN1 recapitulates regulation of translation and deadenylation. *Science* **365**, 825–829
47. Deng, Y., Efremov, A. K., and Yan, J. (2022) Modulating binding affinity, specificity, and configurations by multivalent interactions. *Biophys. J.* **121**, 1868–1880
48. Shrinivas, K., Sabari, B. R., Coffey, E. L., Klein, I. A., Boija, A., Zamudio, A. V., *et al.* (2019) Enhancer features that drive formation of transcriptional condensates. *Mol. Cell* **75**, 549–561.e7
49. Liu, M., Huang, L. Z. X., Smits, A. A., Büll, C., Narimatsu, Y., van Kuppeveld, F. J. M., *et al.* (2022) Human-type sialic acid receptors contribute to avian influenza A virus binding and entry by hetero-multivalent interactions. *Nat. Commun.* **13**, 4054
50. Cushing, P. R., Vouilleme, L., Pellegrini, M., Boisguerin, P., and Madden, D. R. (2010) A stabilizing influence: CAL PDZ inhibition extends the half-life of ΔF508-CFTR. *Angew. Chem. Int. Ed. Engl.* **49**, 9907–9911
51. Roberts, K. E., Cushing, P. R., Boisguerin, P., Madden, D. R., and Donald, B. R. (2012) Computational design of a PDZ domain peptide inhibitor that rescues CFTR activity. *PLoS Comput. Biol.* **8**, e1002477
52. Xie, X., Matsumoto, S., Endo, A., Fukushima, T., Kawahara, H., Saeki, Y., *et al.* (2018) Deubiquitylases USP5 and USP13 are recruited to and regulate heat-induced stress granules through their deubiquitylating activities. *J. Cell Sci.* **131**, jcs210856
53. Pesce, E., Sondo, E., Ferrera, L., Tomati, V., Caci, E., Scudieri, P., *et al.* (2018) The autophagy inhibitor Spautin-1 antagonizes rescue of mutant CFTR through an autophagy-independent and USP13-mediated mechanism. *Front. Pharmacol.* **9**, 1464
54. Kumar, G. S., Gokhan, E., De Munter, S., Bollen, M., Vagnarelli, P., Peti, W., *et al.* (2016) The Ki-67 and RepoMan mitotic phosphatases assemble via an identical, yet novel mechanism. *Elife* **5**, e16539
55. van den Bos, C., Rammes, A., Vogl, T., Boynton, R., Zaia, J., Sorg, C., *et al.* (1998) Copurification of P6, MRP8, and MRP14 from human granulocytes and separation of individual proteins. *Protein Expr. Purif.* **13**, 313–318
56. Clare, D. A., and Lecce, J. G. (1991) Copurification of bovine milk xanthine oxidase and immunoglobulin. *Arch. Biochem. Biophys.* **286**, 233–237
57. de Marco, A. (2021) Recombinant proteins co-expressed and co-purified in the presence of antibody fragments. *Methods Mol. Biol.* **2178**, 93–103
58. El Khouri, M., Catala, M., Seijo, B., Chabal, J., Dardel, F., Tisné, C., *et al.* (2021) Coexpression and copurification of RNA-protein complexes in *Escherichia coli*. *Methods Mol. Biol.* **2323**, 67–73
59. Falke, D., Fischer, M., Ihling, C., Hammerschmidt, C., Sinz, A., and Sawers, G. (2021) Co-purification of nitrate reductase 1 with components of the cytochrome *bcc-aa*$_3$ oxidase supercomplex from spores of *Streptomyces coelicolor* A3(2). *FEBS Open Bio.* **11**, 652–669
60. Markmiller, S., Soltanieh, S., Server, K. L., Mak, R., Jin, W., Fang, M. Y., *et al.* (2018) Context-dependent and disease-specific diversity in protein interactions within stress granules. *Cell* **172**, 590–604.e13
61. Protter, D. S. W., and Parker, R. (2016) Principles and properties of stress granules. *Trends Cell Biol.* **26**, 668–679
62. Riggs, C. L., Kedersha, N., Ivanov, P., and Anderson, P. (2020) Mammalian stress granules and P bodies at a glance. *J. Cell Sci.* **133**, jcs242487
63. Wolozin, B., and Ivanov, P. (2019) Stress granules and neurodegeneration. *Nat. Rev. Neurosci.* **20**, 649–666
64. Tate, J. G., Bamford, S., Jubb, H. C., Sondka, Z., Beare, D. M., Bindal, N., *et al.* (2019) COSMIC: the catalogue of somatic mutations in cancer. *Nucleic Acids Res.* **47**, D941–D947
65. Zhao, Y., Cushing, P. R., Smithson, D. C., Pellegrini, M., Pletnev, A. A., Al-Ayyoubi, S., *et al.* (2018) Cysteine modifiers suggest an allosteric inhibitory site on the CAL PDZ domain. *Biosci. Rep.* **38**, BSR20180231
66. Zhang, H., Zhang, S., He, H., Zhang, C., Chen, Y., Yu, D., *et al.* (2014) RasGAP-derived peptide GAP159 enhances cisplatin-induced cytotoxicity and apoptosis in HCT116 cells. *Acta Pharm. Sin. B* **4**, 128–134
67. Amen, T., Guihur, A., Zelent, C., Ursache, R., Wilting, J., and Kaganovich, D. (2021) Resveratrol and related stilbene-derivatives induce stress granules with distinct clearance kinetics. *Mol. Biol. Cell* **32**, ar18
68. Eiermann, N., Haneke, K., Sun, Z., Stoecklin, G., and Ruggieri, A. (2020) Dance with the devil: stress granules and signaling in antiviral responses. *Viruses* **12**, 984
69. Almutairy, B. K., Alshetaili, A., Anwer, K., and Ali, N. (2021) In silico identification of microRNAs targeting the key nucleator of stress granules, G3BP: promising therapeutics for SARS-CoV-2 infection. *Saudi J. Biol. Sci.* **28**, 7499–7504
70. Luo, L., Li, Z., Zhao, T., Ju, X., Ma, P., Jin, B., *et al.* (2021) SARS-CoV-2 nucleocapsid protein phase separates with G3BPs to disassemble stress granules and facilitate viral production. *Sci. Bull.* **66**, 1194–1204
71. Panas, M. D., Ahola, T., and McInerney, G. M. (2014) The C-terminal repeat domains of nsP3 from the old World alphaviruses bind directly to G3BP. *J. Virol.* **88**, 5888–5893
72. Cristea, I. M., Carroll, J.-W. N., Rout, M. P., Rice, C. M., Chait, B. T., and MacDonald, M. R. (2006) Tracking and elucidating alphavirus-host protein interactions. *J. Biol. Chem.* **281**, 30269–30278
73. Fros, J. J., Domeradzka, N. E., Baggen, J., Geertsema, C., Flipse, J., Vlak, J. M., *et al.* (2012) Chikungunya virus nsP3 blocks stress granule assembly by recruitment of G3BP into cytoplasmic foci. *J. Virol.* **86**, 10873–10879
74. Bradbury, N. A., Jilling, T., Berta, G., Sorscher, E. J., Bridges, R. J., and Kirk, K. L. (1992) Regulation of plasma membrane recycling by CFTR. *Science* **256**, 530–532
75. Bomberger, J. M., MacEachran, D. P., Coutermarsh, B. A., Ye, S., O'Toole, G. A., and Stanton, B. A. (2009) Long-distance delivery of bacterial virulence factors by *Pseudomonas aeruginosa* outer membrane vesicles. *PLoS Pathog.* **5**, e1000382
76. Miller, J. H. (1972) *Experiments in Molecular Genetics*, Cold Spring Harbor Laboratory, Cold Spring Harbor, NY
77. Amacher, J. F., Cushing, P. R., Brooks, L., Boisguerin, P., and Madden, D. R. (2014) Stereochemical preferences modulate affinity and selectivity among five PDZ domains that bind CFTR: comparative structural and sequence analyses. *Structure* **22**, 82–93
78. Amacher, J. F., Cushing, P. R., Bahl, C. D., Beck, T., and Madden, D. R. (2013) Stereochemical determinants of C-terminal specificity in PDZ peptide-binding domains: a novel contribution of the carboxylate-binding loop. *J. Biol. Chem.* **288**, 5114–5126
79. Kabsch, W. (2010) XDS. *Acta Crystallogr. D Biol. Crystallogr.* **66**, 125–132
80. Liebschner, D., Afonine, P. V., Baker, M. L., Bunkóczi, G., Chen, V. B., Croll, T. I., *et al.* (2019) Macromolecular structure determination using X-rays, neutrons and electrons: recent developments in Phenix. *Acta Crystallogr. D Struct. Biol.* **75**, 861–877
81. McCoy, A. J., Grosse-Kunstleve, R. W., Adams, P. D., Winn, M. D., Storoni, L. C., and Read, R. J. (2007) Phaser crystallographic software. *J. Appl. Crystallogr.* **40**, 658–674
82. Emsley, P., Lohkamp, B., Scott, W. G., and Cowtan, K. (2010) Features and development of Coot. *Acta Crystallogr. D Biol. Crystallogr.* **66**, 486–501
83. Pinheiro, J., and Bates, D. (2022) R Core Team. nlme: Linear and Nonlinear Mixed Effects Models. *R package version 3*, 1–160
84. Wickham, H. (2016) *ggplot2: Elegant Graphics for Data Analysis*, Springer-Verlag, New York, NY